An Integrated Framework for Actionable Flood Warnings on Road Structures Using High Resolution Satellite Imagery

Zhouyayan Li[1,4], Bekir Z. Demiray[2,4], Marian Muste[4], Ibrahim Demir[1,3,4]

[1] Department of Civil and Environmental Engineering, University of Iowa
[2] Interdisciplinary Graduate Program in Informatics, University of Iowa
[3] Department of Electrical and Computer Engineering, University of Iowa
[4] IIHR Hydroscience and Engineering, University of Iowa

Abstract

Floods rank among the most devastating natural hazards globally. Unlike many other natural calamities, floods typically occur in densely populated regions, resulting in immediate and long-term adverse impacts on communities, including fatalities, injuries, health risks, and significant economic and environmental losses annually. Traditional flood models, while useful, are constrained by simplifying assumptions, numerical approximations, and a lack of sufficient data for accurate simulations. Recent advancements in data-efficient Digital Elevation Model (DEM) and Digital Terrain Model (DTM) based flood models show promise in overcoming some of these limitations. However, these models' reliance on DEM or DTM data renders them sensitive to the dynamic nature of the Earth's surface. This study investigates the effectiveness of remote sensing imagery for flood inundation mapping, focusing on the role of high-resolution commercial optical PlanetScope images in data-limited scenarios. To address early-stage reflectance issues attributed to the lack of on-board calibration in PlanetScope constellations, we introduced a novel post-processing workflow, the Quantile-based Filling and Refining (QFR). Our results indicate that the initial flood extent maps produced using the widely adopted Normalized Difference Water Index (NDWI) were inferior to manual delineations and comparable to those generated using only the Near-Infrared (NIR) band, which also suffers from reflectance flaws. However, flood maps generated using NIR band data processed with the QFR significantly outperformed manual delineations. This research demonstrates the potential of commercial remote sensing imagery for precise flood inundation mapping, particularly at smaller scales, such as urban areas. Additionally, it underscores the QFR post-processing workflow's effectiveness in enhancing prediction accuracy, offering a streamlined and scalable method for improving flood modeling outcomes.

Keywords: satellite imagery, flood inundation maps, map extraction, image processing, flood forecasting, decision making

1. Introduction

Catastrophic floods rank among the top natural hazards globally due to their frequent occurrence along densely populated river tributaries and coastal regions (Blöschl et al., 2020; NOAA, n.d.). Beyond being a natural phenomenon, flooding represents a significant social and economic threat, causing widespread disruptions and tremendous economic and environmental losses (Alabbad and Demir, 2022). A recent work by Rentschler et al. (2022) indicates that floods impact people across all continents, underscoring their universal reach and severity.

Hydrologic or hydraulic flood models are the major tools used to understand floods, assess the risk and damage, and prepare for future events (Li and Demir, 2022). Although those models have been useful in terms of guiding decision making, they require massive input and need considerable effort in tuning and calibration (Teng et al., 2017; Demir et al., 2022), and therefore are limited to regions with extensive, ready-to-use data coverage. Additionally, as the Earth's surface is constantly changing due to natural factors, human activities, and climate change, the hydraulic conditions change accordingly, which therefore requires to continuously update the data describing the surface and hydraulic conditions. These updates are time- and labor-expensive, therefore even the most developed counties in the world struggle to update these data at a pace that can keep up with the changes. In addition to the outdated data issue, there are still large areas on the Earth where the data are far from sufficient to build hydro-models for flood mapping, which rules out those models of being potential tools to be used to document floods in those data-scarce areas (Li et al., 2024).

Over the past two decades, several breakthroughs have emerged that are especially favorable for data-scarce regions. One of the most eye-catching ones is the introduction of DEM-based models, such as Height Above Nearest Drainage (Nobre et al., 2011), planar models (Teng et al., 2015), GFPLAIN (Nardi et al., 2019). Compared to traditional flood models, the DEM-based models require elevation data, which are public datasets with global coverage are available, as their main input (Hocini et al., 2021; Hu and Demir, 2021). Their model structures are also significantly simpler with just a few parameters to tune. Many of those models, especially HAND, have been proven to be able to generate comparable results with their complex competitors in regions with various surface and hydraulic conditions (Afshari et al., 2018; Li et al., 2023a). Although these DEM-based models may underperform in complex conditions (Godbout et al., 2019), researchers have been working on and have already come up with approaches to improve performance without sacrificing a lot on efficiency (Li et al., 2022).

Despite the fact that DEM-based flood models require far less input data, the DEM data they utilize, especially public datasets, can be significantly outdated. For instance, SRTM, one of the most frequently used global DEM dataset, was first released in 2000 and its latest version (1 arc-second Version 3 void-filled) was released a decade ago (*SRTM – Shuttle Radar Topography Mission | Center for Earth Observation*, n.d.). This makes the other eye-catching advancement in the recent years in flood modeling and mapping domain, remote-sensing (RS) based flood mapping stand-out (Li et al., 2023b). Compared to the DEM-based models, RS-based flood mapping work relies exclusively on remote sensing images (Li and Demir, 2024a). As of today,

there are already several satellite-based Earth observing systems, including Sentinel-1, Sentinel-2, Landsat series, MODIS series, and so on, that provide openly available Earth Observation (EO) images. The global coverage and frequent updates of these systems made RS-based flood mapping increasingly popular to support flood risk and mitigation assessment (Alabbad et al., 2023; Yildirim et al., 2022), particularly in data-scarce regions where other approaches are not available.

Most existing studies so far work with public RS imagery. The resolution of those most widely used public RS images - Sentinel-1 SAR, Sentinel-2 and Landsat optical images, ranges from 10 m to 30 m, and thus has placed certain limitations on the scope of study region. More specifically, the study region cannot be city-level or smaller, as 10 m or 30 m per pixel on the image will be comparatively too coarse for small-scale flood mapping. Commercial EO constellations such as WorldView, RapidEye, and PlanetScope, began operations later than these public sources, but are growing fast over the recent years, both in terms of quantity and quality.

Those commercial RS images often have better spatial and temporal resolution and are therefore more suitable for small-scale applications. However, the quality deficiency of some commercial EO products due to the lack of onboard calibration and other issues in the early stage (Frazier & Hemingway, 2021; Huang & Roy, 2021) making the results prone to errors and less favorable, even though, in some cases, the commercial EO images may be the only accessible source when other public images are not available. Therefore, there are fewer studies that utilize commercial EO images, especially when early-stage image quality issues can compromise results.

Recently, Li & Demir (2024) conducted a study that reported poor results of Sentinel-1 SAR, Sentinel-2, and PlanetScope images in flood mapping in densely vegetated regions because the signals could not penetrate vegetation canopies. In addition to that, the authors noted even worse results from PlanetScope, attributed to reflectance discrepancies caused by the lack of onboard calibration of the PlanetScope constellation. The authors proposed a stronger post-processing approach called Quantile-based Filling & Refining (QFR) to improve the results for densely vegetated regions and discovered that the corrected PlanetScope images not only showed significant improvement but also aligned more closely with the post-processed results from SAR and Sentinel-2 images.

The study proposed a feasible approach to correct deficiencies in PlanetScope images. However, since this approach is relatively new, further validation is necessary to prove the efficacy of the proposed approach. This study will investigate the usefulness of the QFR with two city-level regions that suffered from flooding events in Iowa. PlanetScope images will be used for flood inundation mapping, as there are no commonly used public RS images for these two specific regions during flooding events. The usefulness of the QFR will be evaluated by comparing against manually delineated flood scope and the state-wise reference flood maps. The significancy of this study does not only lie in the results in these two city-level regions but also in investigating the efficacy and usefulness of a newly introduced post-processing approach to handle the quality issues with commercial RS images.

2. Methods

2.1. Case Study

The accuracy of the results produced by numerical models over the range of scales needed for decision making is largely unknown as the available on-the-ground information from measurements and visual observations is scarce and prohibitive expensive to obtain. The success of an effective flood inundation mapping fundamentally depends on the careful selection of study sites and the thorough gathering of all relevant data. This section outlines the systematic approach adopted in our research to identify such locations in Iowa, a region known for multiple flooding in the recent decades (Xiang et al., 2021) The criteria for site selection were comprehensive, with a focus on the presence of bridges, geographical diversity, historical flood data significance, and the presence of reliable sensor data in the area. The ensuing discussion details the rationale behind choosing each site and the strategic compilation of data resources, setting the stage for an in-depth analysis of flood extents and the efficacy of the newly introduced QFR approach.

We identified three sites equipped with bridges and upstream USGS sensors critical for analyzing flood events' impact in close correlation with referenced infrastructure and quantifiable stream variables (i.e., stage and discharge). The selection entails the City of Fredericksburg, Chickasaw County, near a branch of the Wapsipinicon River; the City of Traer, Tama County; and the vicinity of the City of Basset, Chickasaw County, on the Cedar River. Each site's choice was informed by its unique geographical characteristics and historical flood data, underscoring the goal to capture a wide range of flood scenarios. Detailed information on each site's geographical location, bridge specifications, USGS Sensor ID, and flood stage data is systematically presented in Table 1.

Table 1: Information about selected sites for flood event analysis

Site Name	Site Location	Location of Bridge (lat, lng)	USGS Sensor ID	Flood Stage (ft)
Site #1	Fredericksburg, Chickasaw County	(42.97, -92.21)	05421000	12
Site #2	City of Traer, Tama County	(42.20, -92.47)	05464220	12
Site #3	City of Basset, Chickasaw County	(43.07, -92.55)	05458000	10

Upon selecting the sites, we identified flooding times using USGS sensor data accessed through the National Weather Service. Through this step we identified 21 significant flood events across the sites that enabled to carry on a systematic approach in exploring the high-resolution imagery for the most impactful instances of flooding at each site, therefore ensuring the needed detail and relevance to the study. A summary of the flood-related specifications for each site and events is provided in Appendix A1. This table offers a clear overview of the flood events considered in our analysis.

For high-resolution satellite imagery, we utilized PlanetScope from Planet.com, targeting images within a range of one week before to one week after the identified flood dates. This

method was designed to capture the entire progression of each flood event comprehensively. However, as we delved into the data, it became apparent that only two of these sites – Site #1 and Site #2 – had usable high-resolution imagery for a significant flood event each. More specifically, we selected the flood event on July 23, 2017, for Site #1, and the event on March 15, 2019, for Site #2, as only these instances had high-quality imagery available. This limitation in the availability of imagery data for all events at all sites led us to narrow our study's focus to these two locations. Figures 1 and 2 depict the geographical locations of the selected study sites, as well as the precise positions of the bridges within these areas.

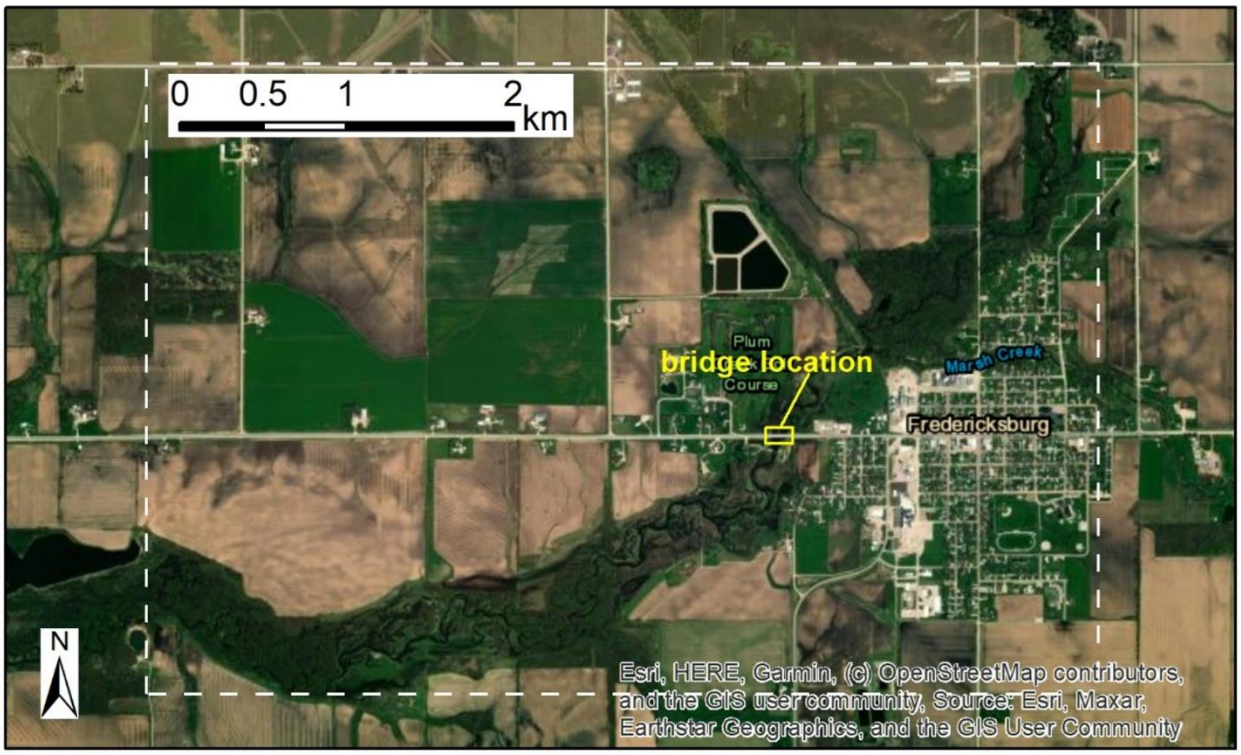

Figure 1. Study site #1 with highlighted bridge location at Fredericksburg, Iowa.

The final stage in our site selection process involved integrating digital elevation models. These models were crucial for our automatic flood map extraction, providing essential insights into the terrain of each site. The process of data collection and analysis ensured that our study was grounded in the most accurate and comprehensive information available, underpinning the creation of a robust foundation for the development of an effective flood inundation mapping used as benchmark in this study.

2.2. Manual Flood Map Extraction

In our research, the first step starts with manually extracting flood maps using high-resolution imagery exclusively from Planet.com. This manual process involved a detailed visual analysis of the imagery to identify and delineate the extent of flooding. Given the high spatial resolution of

Planet's imagery, we could discern subtle variations and anomalies that indicate flooding, although challenges such as cloud cover and similar color patterns in the terrain occasionally required educated guesses to accurately map flood extents.

This manual approach complements automated flood mapping techniques, bringing a critical human element to the interpretation of satellite data. Despite being labor-intensive, it's invaluable in instances where automated algorithms may not fully capture the complexities of flood scenarios, especially in cloud-affected areas. By enhancing the precision of flood mapping through this method, we aim to provide more actionable insights for flood risk management and emergency response planning.

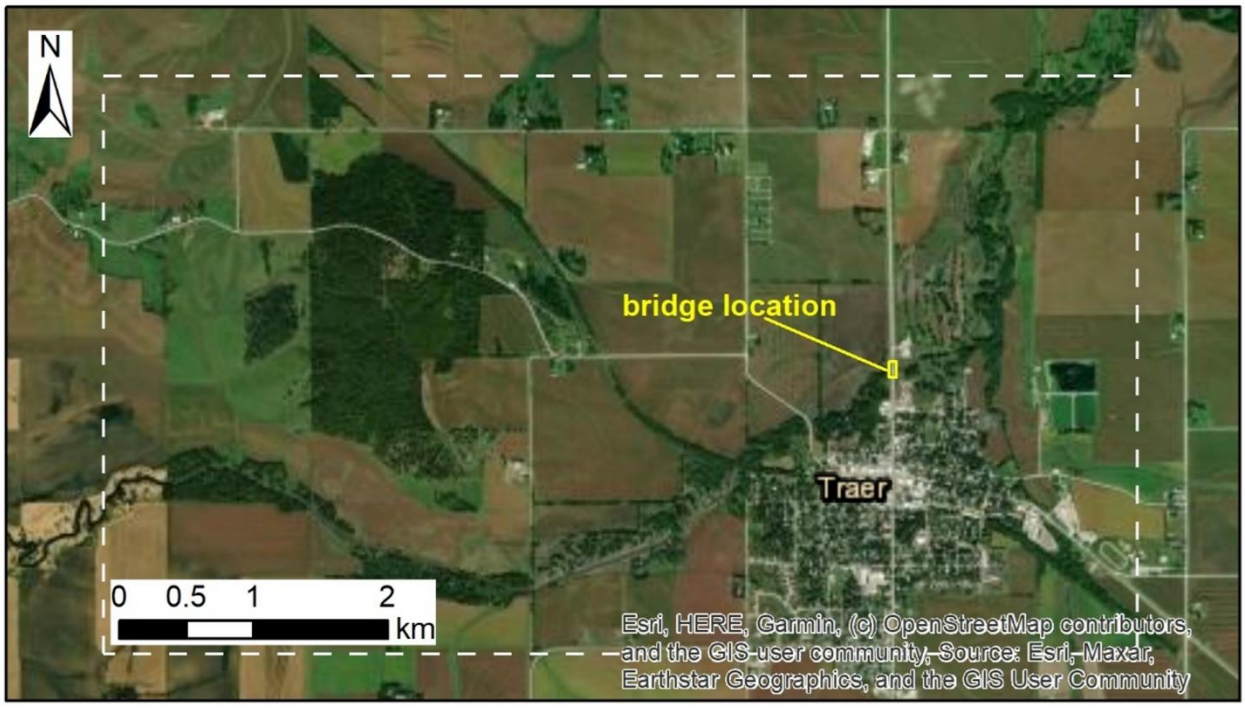

Figure 2. Study site #2 with highlighted bridge location at Traer, Iowa.

2.3. Automated Flood Map Extraction

2.3.1. Otsu Thresholding

Otsu thresholding was proposed by Nobuyuki Otsu (1979). It is an automated histogram analyzing technique that minimizes the differences of samples within groups while maximizing the differences between them (Nobuyuki Otsu, 1979). Being simple and robust, the Otsu method has been widely used in flood inundation mapping where the goal is to classify pixels into dry area (background) and water bodies (foreground) (Moharrami et al., 2021; Pelich et al., 2022; Zhao et al., 2021). In recent years, researchers have proposed improved thresholding methods based on Otsu, such as Bmax Otsu (Cao et al., 2019; Markert et al., 2020), where the main focus is to introduce more flexibility to large-scale classification by allowing multiple thresholds within the entire study area. In our study, as shown in Figures 1 and 2, the study areas are not very large. Therefore, we believe the original Otsu thresholding method should produce results

comparable to its more complex counterparts while requiring fewer computational resources and less time.

2.3.2. QFR Postprocessing

In many cases, due to the data limitations coming from satellite revisit schedules, image resolution, and weather and illumination conditions, we have no other image sources to switch to when the results generated with the existing data are quite dissatisfying. Rather than accepting those bad results or simply discarding everything, we need to investigate with care to see if there are any possibilities for improving the current results. The QFR was introduced following that idea. QFR is a highly structured framework, introduced by Li and Demir (2024b), that provides stronger post-processing to resolve significant systematic classification mismatches in water extent maps due to complex hydraulic conditions and blocking from dense vegetation canopies and clouds. Simple yet robust, QFR has already been seamlessly integrated into an open-access Google Earth Engine application, MultiRS Flood Mapper, introduced by Li and Demir (2024c) to provide global high-resolution flood inundation maps generated using Landsat 8, Sentinel-2, and Sentinel-1 SAR images.

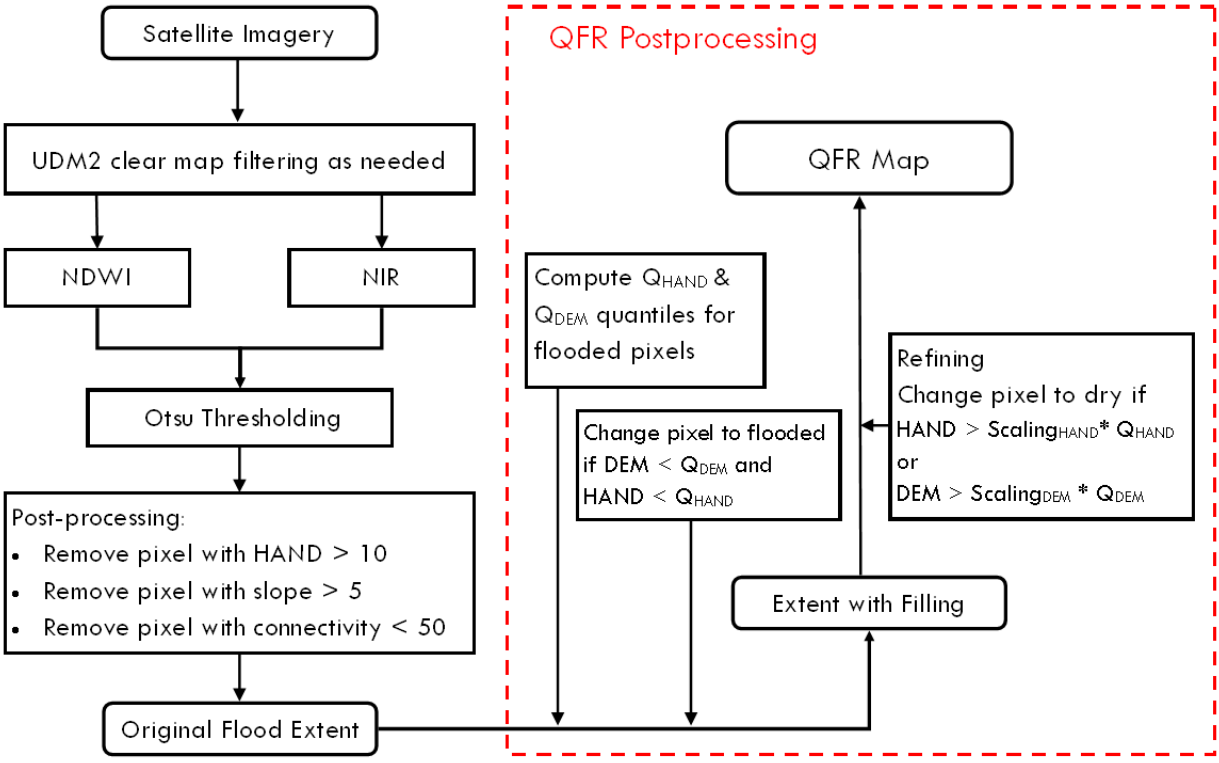

Figure 3. The flood inundation mapping workflow including the QFR postprocessing adopted in this study.

In this study, QFR is adopted to improve quality of the automated flood inundation maps to enhance the automation level of entire flood inundation mapping workflow. Figure 3 depicts the

flood inundation mapping workflow used in this study, where the dash line enclosing the QFR procedure indicates that the QFR is optional. As suggested by the previous works (Li and Demir, 2024b, 2024c), QFR is only necessary if the standard workflow of water body extraction fails to produce satisfying results. It is also worth noting that we have modified the QFR slightly compared to its original version. As mentioned by Li & Demir (2024b), QFR is a highly flexible post-processing workflow in terms of setting up user-defined thresholds. Additionally, all sub-modules are self-explanatory and easy-to-use. Therefore, we removed some inapplicable sub-models and adjusted a few thresholds for improved flexibility and performance. Last but not least, we performed the QFR postprocessing only to the best original flood map, which could be derived using either the NDWI index or the NIR band. The less accurate flood map was discarded.

2.4. Flood Inundation Extent Prediction Evaluation

The manual and automated flood extent maps were compared pixel by pixel with the 100-year flood inundation maps. Since the reference map and the manual maps are vectors, while the automated maps are raster files, we first rasterized those vectors using the scope and pixel resolution of the automated maps. We then adopted the following metrics to measure the similarity between the extracted maps (automated or manual) and the reference map. Accuracy, as given in Equation 1, is the ratio of correct pixels to all pixels on the prediction map (i.e., the manual and automated map). It demonstrates the overall accuracy of the prediction map without distinguishing the prediction classes. Accuracy ranges in [0, 1] with 1 being the best possible value. It calculates as:

$$Accuracy = \frac{TP + TN}{TP + FN + FP + TN} \quad \text{Eq. 1}$$

where TP, TN, FP, and FN are the number of correct flood pixels, correct dry pixels, incorrect flood pixels, and incorrect pixels, respectively. Hit Rate (H), as shown in Equation 2, different from Accuracy, focuses on the positive (flood, in our case) predictions and measures the ratio of correct positive predictions versus all positive pixels in the reference map. Same as Accuracy, H also ranges in [0, 1] with 1 being the best value. H calculates as:

$$H = \frac{TP}{TP + FN} \quad \text{Eq. 2}$$

F1-score (F1), as provided in Equation 2, considers both precision (the accuracy of positive predictions) and recall (the completeness of positive predictions, also H in our case). It ranges in [0, 1] with 1 being the best value. F calculates as:

$$F1 = \frac{2TP}{2TP + FP + FN} \quad \text{Eq. 3}$$

Bias (Equation 4) is the ratio of flood pixels on the prediction map to flood pixels on the reference map. It shows whether the prediction is overestimated or underestimated in general (Li et al., 2022). Bias is a non-negative value with 1 indicating the overestimation and underestimation by the model is equal. As readers can tell, Bias, compared to other indexes introduced above, does not measure the goodness of the prediction but demonstrates the quantitative relationship of two types of incorrect predictions. Bias is calculated as:

$$Bias = \frac{TP + FP}{TP + FN} \qquad \text{Eq. 4}$$

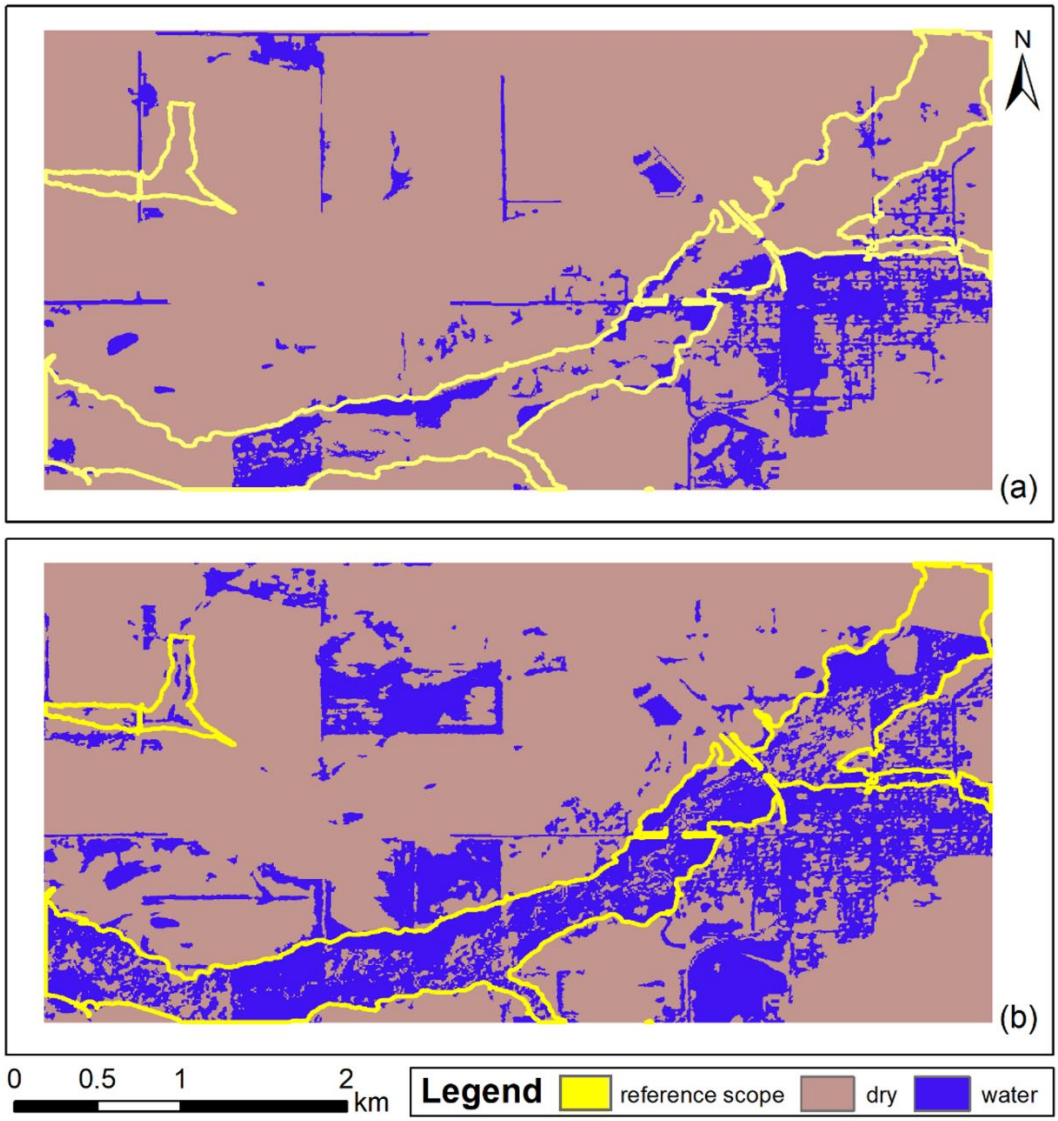

Figure 4. Flood inundation maps generated with NDWI index (a) and the NIR band (b) of PS image in Fredericksburg site.

3. Results and Discussion

3.1. Flood Inundation Maps by Otsu Thresholding

Figure 4 shows the flood inundation map produced by applying Otsu thresholding to the derived NDWI layer and the NIR band of the PS image at the Fredericksburg site. Although the NDWI has been proven to be very useful in water body extraction task by many existing studies in the literature (Ashok et al., 2021; Eid et al., 2020; Zheng et al., 2021), it failed to generate satisfying results in our case. As Figure 4 shows, water bodies derived with the NDWI layer were not even consistent with the shape of the river channel enclosed by the red line. In comparison, the flood map derived from the NIR band shows significant improvement, although it also resulted in more overestimations.

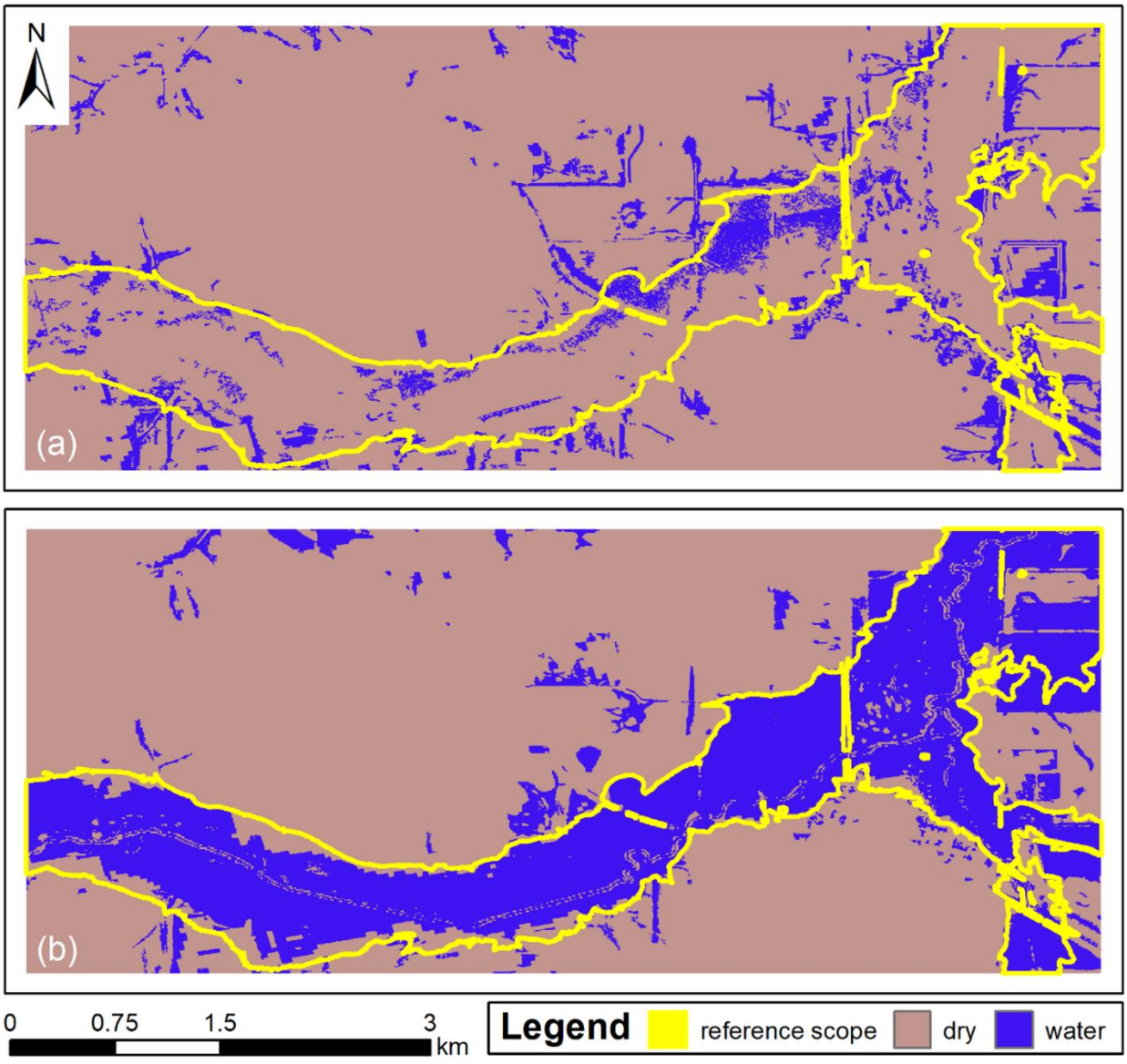

Figure 5. Flood inundation maps generated with NDWI index (a) and the NIR band (b) of PS image in Traer site.

Figure 5 shows the flood maps derived from the NDWI layer and the NIR band of the PS image for the Traer site. Similar to the results observed at the Fredericksburg site, the map derived from the NIR band is also significantly better than the one generated with the NDWI layer. Table 2 lists the evaluation results of the four maps shown in Figures 3 and 4, where F and T represent the Fredericksburg and Traer sites, respectively. The quantitative evaluations shown in Table 2 are consistent with what has been revealed in Figures 4 and 5. The NDWI-derived map falls short of expectations in both sites, as indicated by Accuracy, H, and F1 scores, with a significant underestimation of water bodies highlighted by the Bias score. By contrast, results from the NIR band are noticeably more consistent with the reference map. Additionally, we noticed that the map generated from the NIR band in Fredericksburg is overestimated, while the map for Traer is more balanced in terms of the number over- and under-estimations.

Table 2. Quantitative evaluation of the maps generated with NDWI layer and the NIR band of PS images obtained for Fredericksburg (F) and Traer (T) sites.

	TP (count)	FP (count)	FN (count)	TN (count)	Accuracy	H	F1	Bias
F_NDWI	56,691	151,449	266,961	1,279,465	0.76	0.18	0.21	0.64
F_NIR	204,545	293,271	119,107	1,137,643	0.76	0.63	0.50	1.54
T_NDWI	135,430	158,821	693,478	1,727,991	0.69	0.16	0.24	0.35
T_NIR	670,304	139,869	158,604	1,746,943	0.89	0.81	0.82	0.98

A careful investigation of the image bands attributes these poor-quality flood maps (sub-plot (a) in Figures 4 and 5) to significantly higher NIR values compared to the visible bands including the green band, in both sites. As indicated by NDWI formula, negative NDWIs closer to -1 are possible when the NIR value is much higher than the G value for any given pixel. Our speculation was proved by the two thresholds obtained by the Otsu method. Typically, the NDWI threshold should be around 0 (it may vary slightly among study regions though) for which pixels with larger values indicate the occurrence of flood inundation (McFeeters, 1996; Zheng et al., 2021). By contrast, in our case, the NDWI threshold for Traer was -0.3, while for Fredericksburg, we got an even more unlikely threshold of -0.69. As the threshold is computed by analyzing the histogram of the NDWI values of all pixels, a very negative NDWI value, as seen in this study, indicates that pixels generally have a much higher NIR value compared to the G value, and this is not merely a characteristic of some individual pixels.

Due to the absence of other satellite images on the validation day, we cannot confirm whether these suspected NDWI thresholds are attributable to unusual illumination conditions on those specific two days at the study sites or to any potential quality issues of the PS images. Although, some previous studies have encountered similar situations where the water-body thresholds obtained using PS images were implausibly low (Li & Demir, 2024c), a closer investigation and systematic comparisons are needed before concluding that the quality issue of PS images is the one to blame.

3.2. Improved Inundation Consistency with QFR Post-Processing

Figure 6 depicts the flood maps derived from manual delineation and QFR, along with the detailed locations of TP, FP, TN, and FN when compared to the reference map at the Fredericksburg site. As the QFR procedure adopted in this study contains two major steps (i.e., filling and refining), we showed the flood maps after each step to better demonstrate the effect of each of them. As shown in Figure 6 (a), the manual water extent is well-defined by a simple visual comparison, as opposed to what was depicted in Figure 4. The detailed locations of the four types of classifications (TP, FP, TN, and FN) shown in Figure 6 (b) reveal that the main misclassifications occurred in regions where it was challenging to distinguish between inundated and adjacent dry areas, such as in the top-right corner.

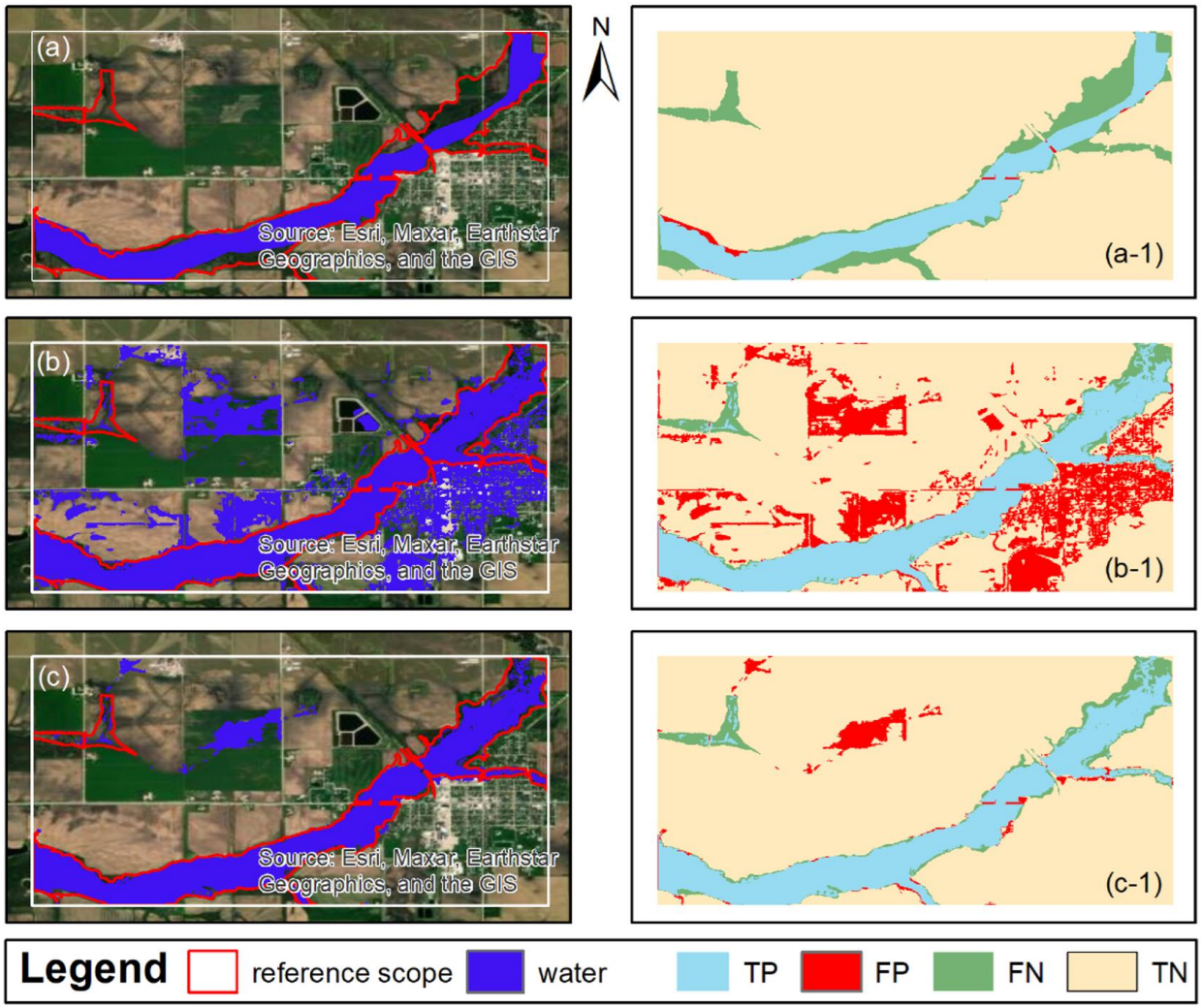

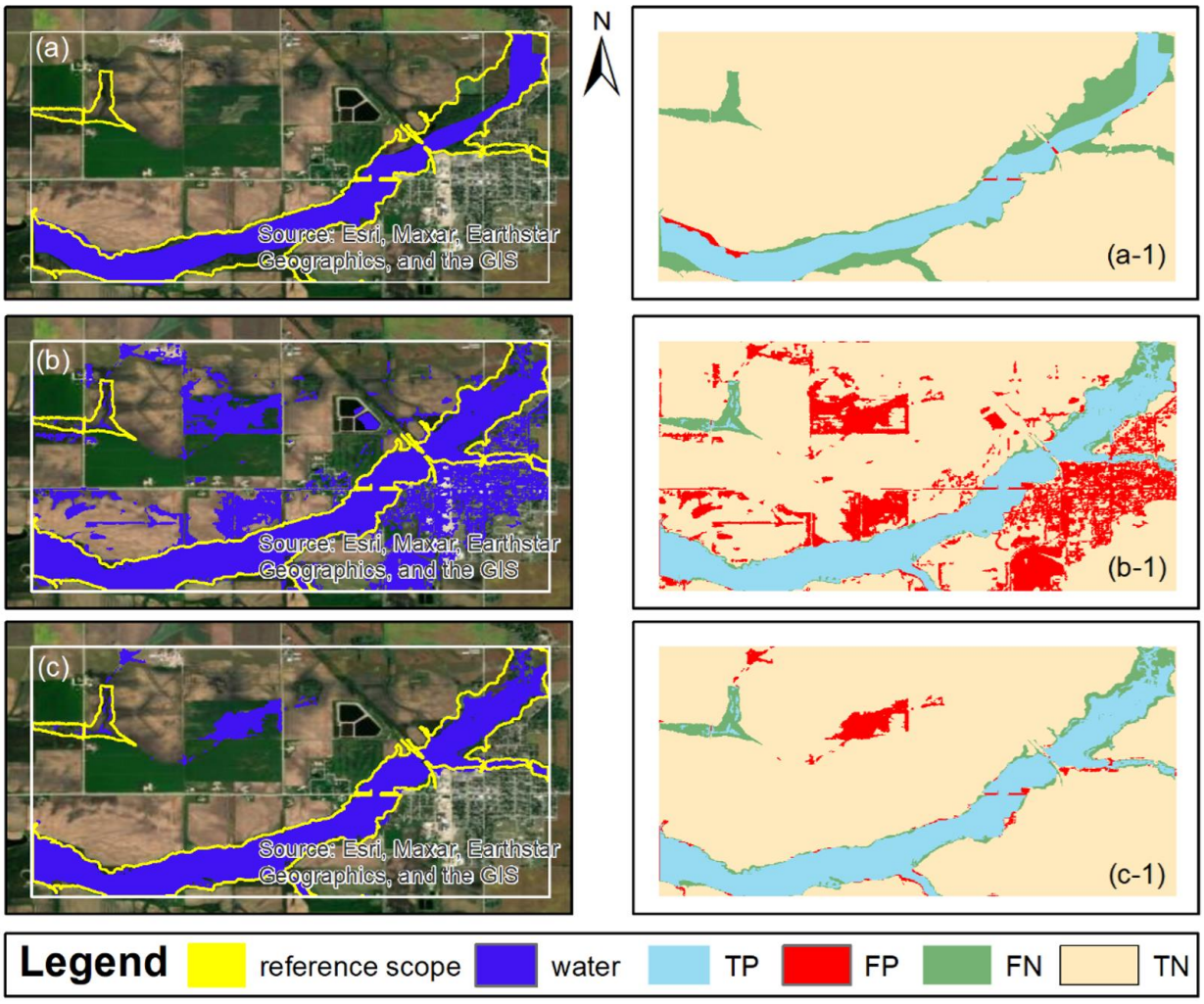

Figure 6. Manual delineation of flood extent (a) and its evaluation against the reference (a-1); automated flood map after the QFR filling step (b) and its evaluation against the reference (b-1); automated flood map after the QFR refining step (done with the QFR post-processing) (c); and its evaluation against the reference (c-1) in Fredericksburg site.

Moreover, underestimations occurred in small branches that are far from the main river channel. As seen in Figure 6 (b), the manual delineation missed small branches in the top-left, middle-right, and at the bottom. This demonstrates that although manual delineations can accurately label the most noticeable water bodies, they lack the attention to detail needed to represent the complex geometry of rivers, leading to some mismatches and a smooth boundary of water bodies. In contrast, automated flood maps are better at capturing those details of the river channel, especially with the QFR flood maps. Compared to Figure 4 (b), the connectivity of flooded pixels in the river channel has been noticeably improved.

Specifically, Figure 6 (b) shows far fewer scattered dry pixels in the main river channel, whereas the water body in Figure 4 (b) is more disconnected due to the large amount of scattered dry pixels. Compared to the manual delineation, the automated map after the filling step (Figure

6 (b-1)) still has far more mismatches, but it does better in those hard-to-distinguish regions we just discussed. The second step of the QFR (i.e., refining) has, as shown in Figure 6 (c) and (c-1), elevated the quality of the automated flood map up to a different level, where not only the overestimations shown in (b-1) have been substantially suppressed but the existing correct classifications were well reserved. In other words, the improvements of the refining step did not come with noticeable hypercorrections.

Figure 7 shows the same comparison for Traer that Figure 6 provides for Fredericksburg. Comparing Figure 7 (a-1) and (b-1), we see that, in Traer, the automated map after the QFR filling step is highly comparable with the carefully delineated manual scope in terms the total amount of mismatches without distinguishing the types (FN or FP) and location. The manual delineation's incapability in distinguishing among nuances or in regions with complex geometries, as discussed above, is also apparent at the Traer site, with noticeable underestimations to the left and along the bottom bank of the main river channel.

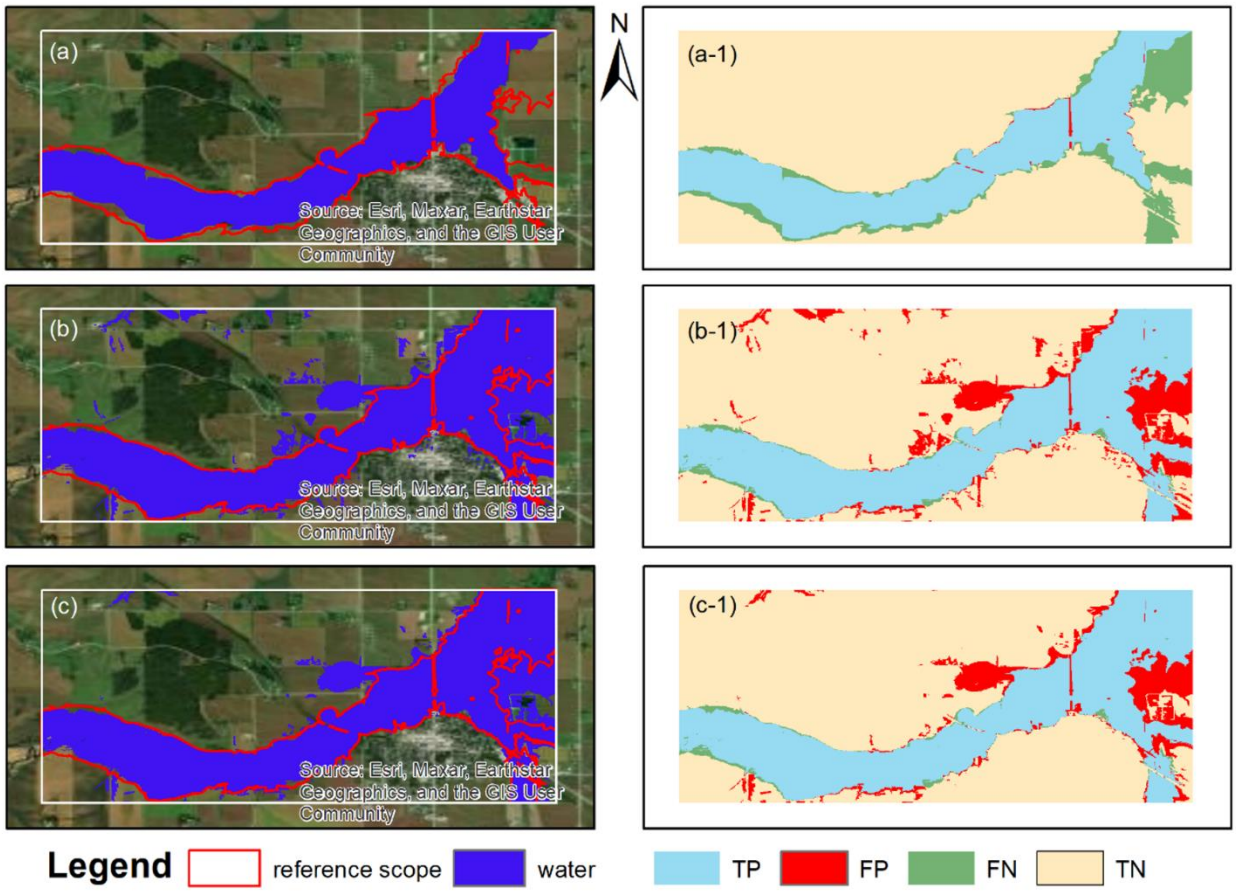

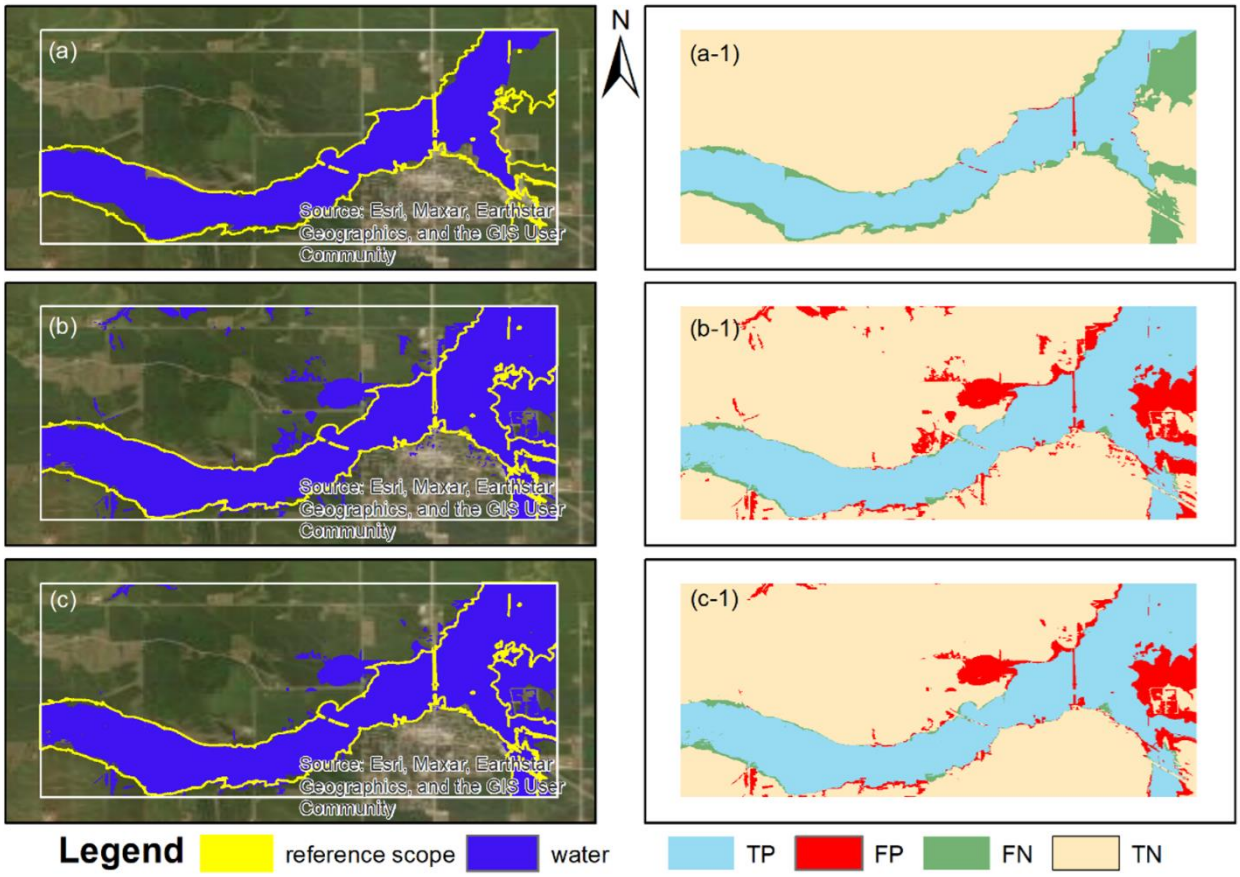

Figure 7. Manual delineation of flood extent (a) and its evaluation against the reference (a-1); automated flood map after the QFR filling step (b) and its evaluation against the reference (b-1); automated flood map after the QFR refining step (done with the QFR post-processing) (c); and its evaluation against the reference (c-1) in Traer site.

The automated flood maps created with QFR filling, and both filling and refining, show fewer differences in Traer than in Fredericksburg. As seen in Figure 7 (c-1), the map refined with QFR managed to get rid of some scattered overestimations in the middle, but most of those overestimations in Figure 7 (b-1) remained unchanged. Given that the flood map derived using the NIR band in Traer was already quite satisfactory, as indicated by the last row of Table 2, it is reasonable that QFR did not bring as significant improvement for maps in Traer compared to those in Fredericksburg.

The thresholds for HAND, slope, and connectivity used in the standard post-processing steps as well as the two quantiles - Q_{HAND} and Q_{DEM}, and the two scaling factors $Scaling_{HAND}$ and $Scaling_{DEM}$, shown in Figure 3, are chosen by referencing to the literature and a few times of trial and error. However, if references exist in any format (i.e., crowded-sourced flood extent observation, formal flood risk map forecasts, and USGS high-water marks), the selection of these values can be fully automated. The quantiles and scaling factors for the two study sites are listed

in Table 3. All these values were obtained or applied to the original flood extent map derived using the NIR band.

Table 3. The quantiles and scaling factors that were used in the QFR post-processing shown in Figure 3 for the two study sites.

Site	**Q_{HAND}**	**Q_{DEM}**	**$Scaling_{HAND}$**	**$Scaling_{DEM}$**
Fredericksburg	0.40	0.50	1.40	1.05
Traer	0.75	0.60	1.50	1.05

Table 4 lists the improved flood inundation mapping after applying the QFR post-processing for the two study sites. As shown in Table 4, the automated maps after QFR post-processing show significant improvement in terms of accuracy and consistency with the reference. The comparison between the original flood map derived with the NIR band and the map after QFR procedure further proves the efficacy of the QFR post-processing. Along with previous studies that demonstrated the efficacy of QFR in resolving mismatches due to complex hydraulic conditions and the blocking from dense vegetation canopies and clouds (Li & Demir, 2024b, 2024c), our study further proves that QFR can also be used to resolve mismatches due to low spectral quality, which could be attributed to unusual external illumination conditions, sensor inaccuracies, and system errors in image generation.

Table 4. lists the quantitative evaluation of the manual flood map and automated maps after the filling and refining of QFR in Fredericksburg (F) and Traer (T).

	TP (count)	**FP (count)**	**FN (count)**	**TN (count)**	**Accuracy**	**H**	**F1**	**Bias**
F_manual	195,713	6,904	127,939	1,424,010	0.92	0.60	0.74	0.63
F_filling	274,052	296,210	49,600	1,134,704	0.80	0.85	0.61	1.76
F_refining	259,849	37,600	63,803	1,393,314	0.94	0.80	0.84	0.92
Compared to F_NIR (%)	27.04	-87.18	-46.43	22.47	23.17	27.04	68.02	-40.25
T_manual	626,403	5,925	202,505	1,880,887	0.92	0.76	0.86	0.76
T_filling	800,359	236,296	28,549	1,650,516	0.90	0.97	0.86	1.25
T_refining	800,054	180,337	28,854	1,706,475	0.92	0.97	0.88	1.18
Compared to T_NIR (%)	19.36	28.93	-81.81	-2.32	3.69	19.36	8.13	21.01

4. Conclusion

In this study, we delineated flood inundation scope with PlanetScope 3-m imagery at Traer and Fredericksburg townships in Iowa, to investigate the usefulness of RS images in validating the model-based flood mapping over a range of scales. Manual delineation and automated delineation using NDWI and the NIR band were compared with each other and against the 100-

year reference flood maps provided by hydrologic models (Ewing et al., 2022). Results show that the reflectance of NIR bands of the image captured for the two study sites was significantly higher than the green bands, which lead to negative NDWI values for many pixels in the scene. The large amount of negative NDWI eventually lead to the failure of the flood map obtained by thresholding on the NDWI. This approach is not only worse than the manual delineation but also inconsistent with the shape of river channels. By contrast, flood maps generated by thresholding on the NIR band were significantly better at both sites.

Results also showcased the efficacy of the QFR post-processing. The maps derived using the NIR band were improved after the QFR application using only DEM and HAND as auxiliary input. Maps created with QFR post-processing were more consistent with the reference map and noticeably better than manual delineations. This study shows that, due to the lack of onboard calibration of PlanetScope's early-stage images, flood maps created using the standard automated extraction workflow with some of the commonly used indexes, such as NDWI, may not be satisfying. Encouraging results are obtained with QFR application that proved to be an efficient streamlined workflow that provides powerful post-processing capabilities that can significantly improve predictions. Not only do post-processed flood maps become more accurate and consistent with the reference, but the entire process is also more efficient and scalable than manual delineations.

These findings underscore the critical importance of selecting appropriate methodologies for flood mapping using remote sensing data. The limitations associated with NDWI thresholding highlight the need for careful consideration of the specific characteristics of the sensor data, including band reflectance properties. Furthermore, the successful application of QFR post-processing emphasizes the potential for advanced computational techniques to enhance the accuracy and reliability of flood maps. This study contributes to the growing body of literature suggesting that while traditional methods have their place, modern algorithmic approaches combined with supplementary geomorphological data like DEM and HAND can offer better outcomes.

Our research also adds to the discourse on the challenges and opportunities inherent in using commercial satellite imagery for hydrological applications. As these data sources continue to evolve, the methodologies we employ must adapt accordingly to leverage their full potential. Future studies should explore integrating multi-temporal analyses and machine learning techniques to refine and validate flood mapping processes further. In conclusion, remote sensing technologies, combined with advanced post-processing methods like QFR, present a promising avenue for enhancing flood mapping precision and operational efficiency. It is imperative for future efforts to pursue improvements in sensor calibration and algorithm development to unlock the full spectrum of benefits these innovations can provide in mitigating the risks associated with flooding.

5. Acknowledgement

The study presented in this report was supported by the Iowa Department of Transportation - SPR-RE22(016)-8H-00. We would like to thank Dave Claman and Jimmy Ellis, who served as members of the technical advisory committee for their support of the project.

6. Disclaimer

During the preparation of this work, the authors used ChatGPT in order to improve the flow of the text, correct any potential grammatical errors, and improve the writing. After using this tool, the authors reviewed and edited the content as needed and take full responsibility for the content of the publication.

7. Reference

Afshari, S., Tavakoly, A. A., Rajib, M. A., Zheng, X., Follum, M. L., Omranian, E., & Fekete, B. M. (2018). Comparison of new generation low-complexity flood inundation mapping tools with a hydrodynamic model. *Journal of Hydrology*, *556*, 539–556. https://doi.org/10.1016/j.jhydrol.2017.11.036

Alabbad, Y., & Demir, I. (2022). Comprehensive flood vulnerability analysis in urban communities: Iowa case study. *International Journal of Disaster Risk Reduction*, 74, 102955.

Alabbad, Y., Yildirim, E., & Demir, I. (2023). A web-based analytical urban flood damage and loss estimation framework. *Environmental Modelling & Software*, *163*, 105670.

Ashok, A., Rani, H. P., & Jayakumar, K. V. (2021). Monitoring of dynamic wetland changes using NDVI and NDWI based landsat imagery. *Remote Sensing Applications: Society and Environment*, *23*, 100547. https://doi.org/10.1016/J.RSASE.2021.100547

Blöschl, G., Kiss, A., Viglione, A., Barriendos, M., Böhm, O., Brázdil, R., Coeur, D., Demarée, G., Llasat, M. C., Macdonald, N., Retsö, D., Roald, L., Schmocker-Fackel, P., Amorim, I., Bělínová, M., Benito, G., Bertolin, C., Camuffo, D., Cornel, D., … Wetter, O. (2020). Current European flood-rich period exceptional compared with past 500 years. *Nature 2020 583:7817*, *583*(7817), 560–566. https://doi.org/10.1038/s41586-020-2478-3

Cao, H., Zhang, H., Wang, C., & Zhang, B. (2019). Operational Flood Detection Using Sentinel-1 SAR Data over Large Areas. *Water 2019, Vol. 11, Page 786*, *11*(4), 786. https://doi.org/10.3390/W11040786

Demir, I., Xiang, Z., Demiray, B., & Sit, M. (2022). Waterbench: a large-scale benchmark dataset for data-driven streamflow forecasting. *Earth System Science Data Discussions*, 2022, 1-19.

Eid, A. N. M., Olatubara, C. O., Ewemoje, T. A., El-Hennawy, M. T., & Farouk, H. (2020). Inland wetland time-series digital change detection based on SAVI and NDWI indecies: Wadi El-Rayan lakes, Egypt. *Remote Sensing Applications: Society and Environment*, *19*, 100347. https://doi.org/10.1016/J.RSASE.2020.100347

Ewing, G., Mantilla, R., Krajewski, W., & Demir, I. (2022). Interactive hydrological modelling and simulation on client-side web systems: an educational case study. *Journal of Hydroinformatics*, 24(6), 1194-1206.

Frazier, A. E., & Hemingway, B. L. (2021). A Technical Review of Planet Smallsat Data: Practical Considerations for Processing and Using PlanetScope Imagery. *Remote Sensing 2021, Vol. 13, Page 3930*, *13*(19), 3930. https://doi.org/10.3390/RS13193930

Godbout, L., Zheng, J. Y., Dey, S., Eyelade, D., Maidment, D., & Passalacqua, P. (2019). Error Assessment for Height Above the Nearest Drainage Inundation Mapping. *Journal of the American Water Resources Association*, *55*(4), 952–963. https://doi.org/10.1111/1752-1688.12783

Hocini, N., Payrastre, O., Bourgin, F., Gaume, E., Davy, P., Lague, D., Poinsignon, L., & Pons, F. (2021). Performance of automated methods for flash flood inundation mapping: a comparison of a digital terrain model (DTM) filling and two hydrodynamic methods. *Hydrology and Earth System Sciences*, *25*(6), 2979–2995. https://doi.org/10.5194/HESS-25-2979-2021

Hu, A., & Demir, I. (2021). Real-time flood mapping on client-side web systems using hand model. Hydrology, 8(2), 65.

Huang, H., & Roy, D. P. (2021). Characterization of Planetscope-0 Planetscope-1 surface reflectance and normalized difference vegetation index continuity. *Science of Remote Sensing*, *3*, 100014. https://doi.org/10.1016/J.SRS.2021.100014

Li, Z., & Demir, I. (2022). A comprehensive web-based system for flood inundation map generation and comparative analysis based on height above nearest drainage. *Science of The Total Environment*, 828, 154420.

Li, Z., & Demir, I. (2024a). Better localized predictions with Out-of-Scope information and Explainable AI: One-Shot SAR backscatter nowcast framework with data from neighboring region. *ISPRS Journal of Photogrammetry and Remote Sensing*, *207*, 92-103.

Li, Z., & Demir, I. (2024b). Flood sequence mapping with multimodal remote sensing under the influence of dense vegetation. *International Journal of Remote Sensing*, *45*(4), 1059–1078. https://doi.org/10.1080/01431161.2024.2305629

Li, Z., & Demir, I. (2024c). MultiRS flood mapper: a google earth engine application for water extent mapping with multimodal remote sensing and quantile-based postprocessing. *Environmental Modelling & Software*, *176*, 106022. https://doi.org/10.1016/J.ENVSOFT.2024.106022

Li, Z., Sermet, M. Y., & Demir, I. (2024). EarthObsNet: A Comprehensive Benchmark Dataset for Data-Driven Earth Observation Image Synthesis. EarthArxiv, 6799. https://doi.org/10.31223/X5GD7J

Li, Z., Duque, F. Q., Grout, T., Bates, B., & Demir, I. (2023a). Comparative analysis of performance and mechanisms of flood inundation map generation using Height Above Nearest Drainage. *Environmental Modelling & Software*, *159*, 105565. https://doi.org/10.1016/J.ENVSOFT.2022.105565

Li, Z., Xiang, Z., Demiray, B. Z., Sit, M., & Demir, I. (2023b). MA-SARNet: A one-shot nowcasting framework for SAR image prediction with physical driving forces. *ISPRS Journal of Photogrammetry and Remote Sensing*, *205*, 176-190.

Li, Z., Mount, J., & Demir, I. (2022). Accounting for uncertainty in real-time flood inundation mapping using HAND model: Iowa case study. *Natural Hazards*, *112*(1), 977–1004. https://doi.org/10.1007/S11069-022-05215-Z

Markert, K. N., Markert, A. M., Mayer, T., Nauman, C., Haag, A., Poortinga, A., Bhandari, B., Thwal, N. S., Kunlamai, T., Chishtie, F., Kwant, M., Phongsapan, K., Clinton, N., Towashiraporn, P., & Saah, D. (2020). Comparing Sentinel-1 surface water mapping algorithms and radiometric terrain correction processing in southeast Asia utilizing Google Earth Engine. *Remote Sensing*, *12*(15), 2469. https://doi.org/10.3390/RS12152469

McFeeters, S. K. (1996). The use of the Normalized Difference Water Index (NDWI) in the delineation of open water features. *International Journal of Remote Sensing*, *17*(7), 1425–1432. https://doi.org/10.1080/01431169608948714

Moharrami, M., Javanbakht, M., & Attarchi, S. (2021). Automatic flood detection using sentinel-1 images on the google earth engine. *Environmental Monitoring and Assessment*, *193*(5), 1–17. https://doi.org/10.1007/S10661-021-09037-7/FIGURES/14

Nardi, F., Annis, A., Baldassarre, G. Di, Vivoni, E. R., & Grimaldi, S. (2019). GFPLAIN250m, a global high-resolution dataset of earth's floodplains. *Scientific Data*, *6*(1), 1–6. https://doi.org/10.1038/sdata.2018.309

NOAA. (n.d.). *Weather Related Fatality and Injury Statistics*. NOAA's National Weather Service. Retrieved January 31, 2022, from https://www.weather.gov/hazstat/

Nobre, A. D., Cuartas, L. A., Hodnett, M., Rennó, C. D., Rodrigues, G., Silveira, A., Waterloo, M., & Saleska, S. (2011). Height Above the Nearest Drainage - a hydrologically relevant new terrain model. *Journal of Hydrology*, *404*(1–2), 13–29. https://doi.org/10.1016/j.jhydrol.2011.03.051

Nobuyuki Otsu. (1979). A Threshold Selection Method from Gray-Level Histograms. *IEEE Trans. Syst. Man Cybern*, *9*(1), 62–66. https://ieeexplore.ieee.org/stamp/stamp.jsp?arnumber=4310076

Pelich, R.-M., Schumann, G., Giustarini, L., Tran, K. H., Menenti, M., & Jia, L. (2022). Surface Water Mapping and Flood Monitoring in the Mekong Delta Using Sentinel-1 SAR Time Series and Otsu Threshold. *Remote Sensing 2022, Vol. 14, Page 5721*, *14*(22), 5721. https://doi.org/10.3390/RS14225721

Rentschler, J., Salhab, M., & Jafino, B. A. (2022). Flood exposure and poverty in 188 countries. *Nature Communications 2022 13:1*, *13*(1), 1–11. https://doi.org/10.1038/s41467-022-30727-4

SRTM – Shuttle Radar Topography Mission | Center for Earth Observation. (n.d.). Retrieved April 13, 2024, from https://yceo.yale.edu/srtm-shuttle-radar-topography-mission

Teng, J., Jakeman, A. J., Vaze, J., Croke, B. F. W., Dutta, D., & Kim, S. (2017). Flood inundation modelling: A review of methods, recent advances and uncertainty analysis. In

Environmental Modelling and Software (Vol. 90, pp. 201–216). https://doi.org/10.1016/j.envsoft.2017.01.006

Teng, J., Vaze, J., Dutta, D., & Marvanek, S. (2015). Rapid Inundation Modelling in Large Floodplains Using LiDAR DEM. *Water Resources Management*, *29*(8), 2619–2636. https://doi.org/10.1007/s11269-015-0960-8

Xiang, Z., Demir, I., Mantilla, R., & Krajewski, W. F. (2021). A regional semi-distributed streamflow model using deep learning. EarthArxiv, 2152. https://doi.org/10.31223/X5GW3V

Yildirim, E., Just, C., & Demir, I. (2022). Flood risk assessment and quantification at the community and property level in the State of Iowa. *International journal of disaster risk reduction*, *77*, 103106.

Zhao, J., Pelich, R., Hostache, R., Matgen, P., Wagner, W., & Chini, M. (2021). A large-scale 2005–2012 flood map record derived from ENVISAT-ASAR data: United Kingdom as a test case. *Remote Sensing of Environment*, *256*, 112338. https://doi.org/10.1016/J.RSE.2021.112338

Zheng, Y., Tang, L., & Wang, H. (2021). An improved approach for monitoring urban built-up areas by combining NPP-VIIRS nighttime light, NDVI, NDWI, and NDBI. *Journal of Cleaner Production*, *328*, 129488. https://doi.org/10.1016/J.JCLEPRO.2021.129488

Appendix

Appendix 1: Flood Event Data for Selected Sites

Site #1		
Event Date	**Stage (ft)**	**Acceptable**
08/31/2021	13.95	Yes
06/10/2020	12.01	Yes
03/15/2019	13.37	Yes
09/05/2018	16.86	Yes
07/23/2017	15.43	Yes
09/25/2016	19.29	Yes
05/29/2015	7.35	No
06/20/2014	13.21	Yes
05/31/2013	14.46	Yes
05/09/2012	6.84	No
03/02/2011	9.40	No
07/24/2010	18.77	Yes
Site #2		
03/09/2021	5.45	No
06/23/2020	17.11	Yes
03/15/2019	15.93	Yes
09/02/2018	12.70	Yes

04/16/2017	6.04	No
01/20/2017	9.28	No
12/16/2015	10.69	No
06/21/2015	7.38	No
07/01/2014	14.13	Yes
05/27/2013	16.21	Yes
04/15/2012	5.83	No
02/18/2011	8.03	No
03/12/2010	12.34	Yes
Site #3		
07/22/2017	13.56	Yes
09/24/2016	13.96	Yes
08/25/2016	15.55	Yes
05/21/2013	18.41	Yes
03/24/2011	10.31	Yes
03/13/2010	13.16	Yes